Available online at www.sciencedirect.com
ScienceDirect
ELSEVIER
Nuclear Physics A 786 (2007) 47–70
NUCLEAR PHYSICS A

Signs of dynamical effects for Cd, Sn, Te, Xe, Ba and Sm nuclear charge radii

J. Libert, B. Roussière *, J. Sauvage

Institut de Physique Nucléaire, CNRS-IN2P3 and Université Paris Sud, F-91406 Orsay Cedex, France

Received 21 December 2006; received in revised form 29 January 2007; accepted 29 January 2007

Available online 1 February 2007

Abstract

The experimental charge radius values along Cd, Sn, Te, Xe, Ba and Sm isotopic series have been extracted from isotope shift measurements using different methods to calibrate the electronic factor and mass shift effects. Static and dynamic charge radii have been calculated in the framework of a microscopic configuration mixing approach on the ground of Hartree–Fock–Bogoliubov solutions obtained with the D1S Gogny effective nucleon–nucleon interaction. Low-energy spectroscopic observables have also been obtained. The theoretical and experimental results are compared and discussed. It is shown that dynamical effects must be taken into account especially for γ-soft and weakly deformed nuclei.

PACS: 21.10.Ft; 21.10.Ky; 21.10.Re; 21.60.Jz; 21.60.Ev; 23.20.-g; 36.10.Dr

Keywords: Cd, Sn, Te, Xe, Ba and Sm isotopes; Exotic nuclei; Nuclear charge radius; Level energy; Transition probability; Isotope shift; Muonic atom spectroscopy; Optical spectroscopy; Nuclear microscopic model

1. Introduction

The charge radii of nuclei, r_c, and their variations along isotopic series provide key information on the nuclear matter behaviour. For example, they can reveal magic numbers and bring out changes in the nuclear deformation between either neighbouring nuclei or different states inside the same nucleus. They constitute hence one of the basic nuclear properties that any nuclear model must be able to well describe.

* Corresponding author. Tel.: +33 1 69156265; fax: +33 1 69156470.
E-mail address: roussier@ipno.in2p3.fr (B. Roussière).

0375-9474/$ – see front matter
doi:10.1016/j.nuclphysa.2007.01.089

The most precise nuclear r_c values have been obtained by use of the muonic atom spectroscopy method. They have been determined for almost all elements using the muon factories, but only for the stable isotopes. The most recent and precise results so obtained have been reviewed by Fricke et al. [1]. To study the r_c evolution through a large number of isotopes, we must also use the numerous results concerning the mean square charge radius changes, $\delta\langle r_c^2\rangle$, yielded by the optical method and choose the r_c value of a stable mass as a reference value.

For the tin isotopes, it was recently shown that the parabolic shape of the r_c curve against the neutron number could be explained by important dynamical effects [2–5]. The purpose of the present work is to study the role played by these dynamical contributions as the proton number moves away from $N = 50$. The data already known [6,7] led us to choose the following elements: Cd, Sn, Te, Xe, Ba and Sm.

In muonic atom spectroscopy the uncertainty on the extracted values is almost only due to the nuclear polarization corrections whereas in optical spectroscopy, to deduce the $\delta\langle r_c^2\rangle$ values from the isotope shift measured, one has to determine the electronic factor F of the optical transition as well as the part of the isotope shift due to the mass difference or mass shift MS. Various ways are currently used to get the F and MS values, which may provide slightly different slopes of the $\delta\langle r_c^2\rangle$ and r_c curves. Therefore, prior to compare nuclear model predictions with the experimental r_c curves, a very careful and critical analysis of the data has to be performed and discussed. This tricky problem will be widely treated in Section 2. The nuclear model, taking into account or not the dynamical effects, used in this work will be presented in Section 3. The comparison between experimental and theoretical results will be shown and discussed in Section 4. Lastly, the conclusions will be drawn in Section 5.

2. Determination of the experimental charge radii of Cd, Sn, Te, Xe, Ba and Sm nuclei

Laser spectroscopy is the only experimental method giving access, from the isotope shift, to the change in the mean square charge radius through long isotopic chains including stable and unstable nuclei. The isotope shift is the displacement of the center of gravity of the hyperfine spectrum between two neighboring isotopes. When the number of neutrons varies, changes are induced in the atom, namely in the reduced mass of the nucleus plus electron system, in the correlations between the electrons and in the charge distribution inside the nucleus giving rise to the normal mass shift ($\delta\nu_{\mathrm{NMS}}^{AA'}$), the specific mass shift ($\delta\nu_{\mathrm{SMS}}^{AA'}$) and the field shift ($\delta\nu_{\mathrm{FS}}^{AA'}$). The mass shift dominates in light nuclei and is small in heavy elements [6]. The normal and specific mass shifts depend in the same way on the atomic masses:

$$\delta\nu_{\mathrm{MS}}^{AA'} = \delta\nu_{\mathrm{NMS}}^{AA'} + \delta\nu_{\mathrm{SMS}}^{AA'} = (N+S)\frac{A'-A}{AA'} = M\frac{A'-A}{AA'}.$$

The normal mass shift is easy to calculate, since N is given by the simple formula: $N = \frac{\nu_i}{1836.1}$ [8], where ν_i is the atomic transition energy. On the other hand, the specific mass shift is very difficult to calculate. For pure $s \rightarrow p$ or $s^2 \rightarrow sp$ transitions, it has been shown that $|S| \leqslant N$ [8]. But when d or f electrons are involved in the transition, S can be of the order of $10 \times N$ or more.

The change in the mean square charge radius is related to the field shift by:

$$\delta\nu_{\mathrm{FS}}^{AA'} = \mathrm{F} \times \lambda^{AA'} = \mathrm{F} \times \mathrm{k} \times \delta\langle r_c^2\rangle^{AA'},$$

where F is the electronic factor of the atomic transition, λ the nuclear parameter given by:

$$\lambda = \delta\langle r_c^2\rangle^{AA'} + (C_2/C_1)\delta\langle r_c^4\rangle^{AA'} + (C_3/C_1)\delta\langle r_c^6\rangle^{AA'} + \cdots$$

and k a correcting factor calculated using the C_n Seltzer coefficients [9,10]. Usually the F factor is obtained from semi-empirical calculations using the Goudsmit–Fermi–Segré formula to evaluate the change of the electronic charge density at the nucleus. Relativistic calculations using Dirac–Fock or multiconfiguration Dirac–Fock methods are also used to determine F. Results obtained by these different methods can differ by 10% to 30% [6].

An alternative way to determine both the electronic F factor and the specific mass shift is by using King plot analysis [11]. In this case, the modified shifts in the optical line under study are plotted against the modified shifts in another line advisably chosen, for instance corresponding to a pure and simple configuration for which the specific mass shift can be estimated to be negligible and the F factor accurately calculated. Such a plot gives a straight line, its intercept is related to the specific mass shift and its slope equal to the ratio of the F factors.

The King plot analysis is also applied with data obtained from other experimental methods, such as the X-ray isotope shifts and the change in the mean square charge radius deduced from electron scattering or muonic experiments. It is worth noting that this type of experiments has been only performed on stable isotopes since it requires several tens of milligrams of target material. Using the muonic isotope shifts is not directly suitable because the difference of muonic level energy does not depend on $\delta\langle r^2\rangle$ but on $\delta\langle r^k e^{-\alpha r}\rangle$. In the case of K-ray isotope shifts, the nuclear charge distribution investigated is the same as in optical isotope shifts but the experimental errors are too important to calibrate reliably the optical isotope shift measurements. In the same way, the accuracy obtained for the charge radius in electron scattering experiment is too low to allow the determination of the F factor and specific mass shift via a King plot analysis. However, electron scattering measurements give access to the radial dependence of the charge distribution. This result can be used to extract the charge radius from the very precise and model-independent Barrett radius obtained in muonic experiments. Such a method using the $\delta\langle r_c^2\rangle$ values resulting from a combined analysis of muonic atom and electron scattering data has been proposed by Fricke et al. to calibrate the optical isotope shift measurements and applied for eight elements (Ca, Kr, Sr, Zr, Mo, Sm, Gd, Pb) [1]. However, by lack of electron scattering data, this combined analysis cannot be used for any isotope series. Nevertheless, in principle, muonic experiments give access to the better charge radius values available for the stable nuclei, in spite of the uncertainty on the calculated nuclear polarization corrections that limits their accuracy. The compilation made by Fricke et al. summarizes the results from muonic experiments performed on almost all stable nuclei and provides a consistent set of charge radius values for these stable isotopes [1]. The isotopic series we are interested in (Cd, Sn, Te, Xe, Ba and Sm), located on both sides of the magic tin nuclei, have many stable isotopes (8, 10, 8, 9, 7 and 7, respectively). Thus, we have used the charge radius values of these stable isotopes to calibrate the isotope shift measurements performed by optical spectroscopy. Our aim is to obtain the most consistent and reliable charge radius values over long isotopic chains in order to perform very stringent comparison with theoretical calculations over a wide range of nuclei. In a first step to estimate the possible remaining uncertainty of the method, we compare the charge radius values determined using the calibration on the muonic data with those obtained with the other methods currently used. The charge radius values obtained from different methods are reported in Tables 1–6 of Appendix A.

2.1. Cadmium isotopes

We have evaluated the charge radii in three ways. Firstly we started from the $\delta\langle r_c^2\rangle$ values given in Ref. [6]. These values have been obtained from the experimental data of Ref. [12]

using a factor F ($F_{SE} = 3.91$ GHz/fm^2) determined semi-empirically and we have deduced the charge radii taking as reference the value of the ^{114}Cd stable isotope known from the Fricke et al. compilation Ref. [1]. The second estimation has consisted in determining new values for the electronic factor and the specific mass shift by doing a King plot between the optical isotope shifts measured for the stable isotopes in the $5s^2\ ^1S_0 \rightarrow 5s\ 5p\ ^3P_1$ transition at 326.1 nm [6,12] and the charge radius values reported in Ref. [1]: $F_\mu = -4.37 \pm 0.18$ GHz/fm^2 and $S/N = 2.43 \pm 0.35$ with $k = 0.977$. Then we have used these F and S/N values to calculate, from the $^{102-120}$Cd isotope shifts of Refs. [6,12], new $\delta\langle r_c^2\rangle$ values and the corresponding charge radii taking the same reference, ^{114}Cd. Lastly the comparison between the experimental isotope shifts and the $\delta\langle r_c^2\rangle$ values extracted from Ref. [1] for the stable nuclei has allowed us to determine the specific mass shift ($S/N = 2.15 \pm 0.18$) when the value of the electronic F factor obtained in Dirac–Fock calculations is used ($F_{DF} = -4.16$ GHz/fm^2, Refs. [10,12]). From these $\delta\langle r_c^2\rangle$ values we have obtained a third set of r_c data taking again as reference r_c (^{114}Cd).

2.2. Tin isotopes

The isotope shifts have been measured from $A = 110$ up to 132 using the $5p^2\ ^3P_0 \rightarrow 5p\ 6s\ ^3P_1$ transition at 286.3 nm [5,13]. In Ref. [13], the electronic factor has been calculated by Baird et al. [14] within a semi-empirical approach ($F_{SE} = 3.3 \pm 0.3$ GHz/fm^2), a $k = 1$ value has been used and the specific mass shift has been evaluated from the $\delta\langle r_c^2\rangle^{124,116}$ value obtained from isotope shift measurement of the K_α transition. In Ref. [5], a King plot has been performed between the optical isotope shift and the muonic $\delta\langle r_c^2\rangle$ values measured for the stable isotopes and reported in Ref. [15], this led to: $F_{\mu 1} = 3.30 \pm 0.27$ GHz/fm^2 with $k = 0.975$ and $S/N = -2.33 \pm 0.35$. We have obtained a new determination of F and S/N by performing a similar King plot analysis using the same optical isotope shift values but the muonic $\delta\langle r_c^2\rangle$ values reported for the stable isotopes by Fricke et al.: $F_{\mu 2} = 2.04 \pm 0.2$ GHz/fm^2 with $k = 0.975$ and $S/N = -0.78 \pm 0.32$. The fourth estimation of the electronic factor, given in Ref. [16] ($F_{DF} = 2.39 \pm 0.27$ GHz/fm^2), has been deduced from a King plot with results from another optical transition for which F was obtained using Dirac–Fock calculations. The specific mass shift has been evaluated from the $\delta\langle r_c^2\rangle^{124,116}$ value measured from the K_α-transition isotope shift ($S/N = -1.04$) and a $k = 1$ value has been used. From these sets of $\delta\langle r_c^2\rangle$ data, we have calculated the charge radii taking as reference the value reported in Ref. [1] for ^{120}Sn, except for the $\delta\langle r_c^2\rangle$ values obtained from $F_{\mu 1}$. In this case, for a consistence purpose, we have used the r_c value given in Ref. [15] for ^{120}Sn.

2.3. Tellurium isotopes

The neutron-rich tellurium isotopes have been recently studied by laser spectroscopy using the $5p^4\ ^3P_2 \rightarrow 5p^3\ 6s\ ^3S_1$ transition at 214.3 nm [17,18]. In this work the electronic factor and the specific mass shift have been determined by performing a King plot between the preliminary optical isotope shifts and the $\delta\langle r_c^2\rangle$ values obtained from muonic experiment [19]: $F_{\mu 1} = 4.66 \pm 0.86$ GHz/fm^2 with $k = 0.974$ and $S/N = -1.89 \pm 0.33$. Starting from the same optical isotope shift values we have done a second determination of the electronic factor and specific mass effect using the muonic $\delta\langle r_c^2\rangle$ values reported in Ref. [1]: $F_{\mu 2} = 3.78 \pm 0.48$ GHz/fm^2 with $k = 0.974$ and $S/N = -1.73 \pm 0.37$. Then we have calculated the resulting charge radii taking as reference the ^{130}Te charge radius in the first case from [19] and in the second case from Ref. [1].

2.4. Xenon isotopes

The optical isotope shifts have been measured from $A = 116$ up to 146 in the $5p^5\,6s\,[\frac{3}{2}]_2 \rightarrow 5p^5\,6p\,[\frac{3}{2}]_2$ transition at 823.2 nm [20]. The $\delta\langle r_c^2\rangle$ values have been obtained using the electronic factor calculated in semi-empirical approach ($F_{SE} = -2.32$ GHz/fm^2 [6]) and assuming the specific mass shift to be zero with an error of $\pm$ the normal mass shift. Using the $\delta\langle r_c^2\rangle$ given in Ref. [20] and taking as reference the ^{136}Xe charge radius reported in Ref. [1] we have calculated the charge radii from ^{116}Xe up to ^{146}Xe. We have determined new values for the electronic factor and the specific mass shift by doing a King plot of the optical isotope shifts [20] versus the $\delta\langle r_c^2\rangle$ values reported in Ref. [1]: $F_\mu = -1.56 \pm 0.11$ GHz/fm^2 with $k = 0.972$ and $S/N = 0.192 \pm 0.266$. Then we have calculated the corresponding $\delta\langle r_c^2\rangle$ from $A = 116$ up to 146 and deduced the charge radii taking again as reference the ^{136}Xe charge radius value reported in Ref. [1].

2.5. Barium isotopes

The optical isotope shifts have been measured from $A = 120$ up to $A = 148$ using two transitions: the $6s^2\,{}^1S_0 \rightarrow 6s\,6s\,{}^1P_1$ transition at 553.6 nm and the BaII D2 line at 455.4 nm (see the laser spectroscopy studies listed in Ref. [6]). In the following we will concentrate on the 553.6 nm transition because, in this case, the electronic factor has been obtained not only from semi-empirical approach but also in multiconfiguration Dirac–Fock calculations [10]. We have used three different methods to estimate the Ba charge radii. Firstly starting with the $\delta\langle r_c^2\rangle$ values from Ref. [6], we have calculated the charge radii taking as reference the r_c value reported in Ref. [1] for ^{138}Ba. The $\delta\langle r_c^2\rangle$ values given in Ref. [6] have been obtained with the following semi-empirical electronic factor and specific mass shift: $F_{SE} = -3.929$ GHz/fm^2 and $S/N = 0$. Secondly we have performed a King plot using the optical isotope shifts measured for the stable isotopes [22] and the charge radius values obtained from muonic experiments and reported in Refs. [21] or [1], this led using $k = 0.97$ to $F_{\mu 1} = -3.163 \pm 0.144$ GHz/fm^2 and $S/N = -0.707 \pm 0.109$ or $F_{\mu 2} = -3.897 \pm 0.189$ GHz/fm^2 and $S/N = 2.649 \pm 0.27$, respectively. Using the $\delta\nu$ values measured from $A = 122$ to $A = 146$ in the 553.6 nm transition [22,23], we have deduced the $\delta\langle r_c^2\rangle$ values corresponding to these electronic factors and specific mass shift effects and then the r_c values taking as reference the ^{138}Ba charge radius [1,21]. Finally we have evaluated the specific mass shift corresponding to the electronic factor obtained in multiconfiguration Dirac–Fock calculations ($F_{MCDF} = -2.996$ GHz/fm^2 [10]) by comparing the $\delta\nu$ values and the muonic $\delta\langle r_c^2\rangle$ values for the stable isotopes: $S/N = 0.1 \pm 1.1$. A new set of r_c data has been obtained taking as reference the charge radius given for ^{138}Ba in Ref. [1].

2.6. Samarium isotopes

Many laser spectroscopy studies have been performed in the samarium isotopes, they have been summed up in Ref. [6]. The optical isotope shifts have been measured from $A = 138$ to 145 using the $4f^6\,6s^2\,{}^7F_2 \rightarrow 4f^6\,6s\,6p\,{}^5G_2$ transition at 600.42 nm [24] and from $A = 146$ to 154 using the $4f^6\,6s^2\,{}^7F_1 \rightarrow 4f^6\,6s\,6p\,{}^7F_0$ transition at 570.68 nm [25]. The isotope shifts of the stable isotopes have been performed extensively, in 15 lines of the SmI spectrum including the 570.68 nm [26]. Thus for this transition we could carry out a King plot analysis using the optical shift and the muonic $\delta\langle r_c^2\rangle$ values given either in Refs. [27,28] or in Ref. [1], this led, using $k = 0.963$, to $F_{\mu 1} = -2.82 \pm 0.14$ GHz/fm^2 and $S/N = -16.37 \pm 1.84$ or $F_{\mu 2} = -2.48 \pm$

0.23 GHz/fm^2 and $S/N = -18.79 \pm 3.01$, respectively. Moreover, for this transition, Fricke et al. have performed a combined analysis of the optical isotope shifts and of the data obtained from muonic atom and electron scattering experiments, which led to $F_{\mu e^-} = -3.86 \pm 0.86$ GHz/fm^2 and $S/N = 0.4 \pm 1.3$. In the 600.42 nm transition, only the isotope shift of the ^{144,147}Sm stable nuclei has been measured, which is insufficient for a calibration using the muonic data. Finally the charge radius values in Sm have been calculated in four ways. Firstly, we have used the semi-empirically determined $\delta\langle r_c^2\rangle$ values given in Ref. [6] for $A = 138$–154 and taken as reference the charge radius of ^{144}Sm reported in Ref. [1]. For $A = 144$–154, we have evaluated the charge radii from the isotope shifts measured in the 570.68 nm transition and the F and S/N values resulting from the King plots performed using either the muonic atom data or the combined analysis. The charge radius of the reference nucleus, ^{144}Sm, was taken from Ref. [1], except when the muonic data used for the King plot were those of Refs. [27,28]. In this case, in order to be consistent we have used the ^{144}Sm r_c value reported in Ref. [27].

The charge radius values obtained as indicated above are presented in Fig. 1. Before $N = 82$ the charge radii obtained using semi-empirical F factors are systematically higher than those using the F factors determined by a King plot analysis between the optical isotope shifts and the muonic $\delta\langle r_c^2\rangle$ values for the stable isotopes. The contrary is observed after $N = 82$. However the scattering of the values is not very important and one can wonder whether the error bars are underestimated. For instance, in case of Cd, the possible systematic error on $\delta\langle r_c^2\rangle$ due to the uncertainty in the specific mass shift effect and F factor has been estimated and is indicated in Ref. [12]. Taking into account these systematic errors results in multiplying by a factor of 5 the error bars in the charge radius as compared with the ones reported in Table 1 column 3, and makes this radius value set consistent with the two others drawn in Fig. 1.

It is in the Xe isotope series that the larger differences are observed between the charge radius sets. But the information on the laser-spectroscopy and muonic-atom experiment results is scanty; in particular the charge radius values from muonic-atom experiment are only available in the compilation of Fricke et al. [1]. However we can see in Fig. 1 that the differences in charge radii between the two data sets are less than or around one per cent. On the other hand, analysing, for different N values the evolution of the charge radius as a function of Z, one can conclude that the true charge radius values lie somewhere between the values labelled F_{SE} and those labelled F_μ.

For Sn, Te, Ba and Sm, two charge radius sets are available for the stable isotopes from muonic-atom experiment, leading to two determinations of the F factor and specific mass shift effect. One can note that there is a compensation between these two parameters since the charge radius values obtained over the whole isotope series remain very similar even when the F and S/N factors are significantly different.

In the following, for the comparison with theory, in a first step we will use the charge radius values labelled F_μ or $F_{\mu 2}$ in Fig. 1 or Tables 1–6. They present the advantage of consistency since they have been obtained applying the same method for the determination of the F factor and specific mass shift effect, using in all cases the charge radii reported for the stable isotopes in the compilation by Fricke et al. [1]. For $^{138-143}$Sm that have not been studied with the same optical transition than the heavier isotopes, we will use the charge radius values from the data set labelled F_{SE}. Finally it is worth noting that the table of nuclear charge radii published by Angeli [29] supports quite well the data sets that we have chosen to compare with the results of calculations.

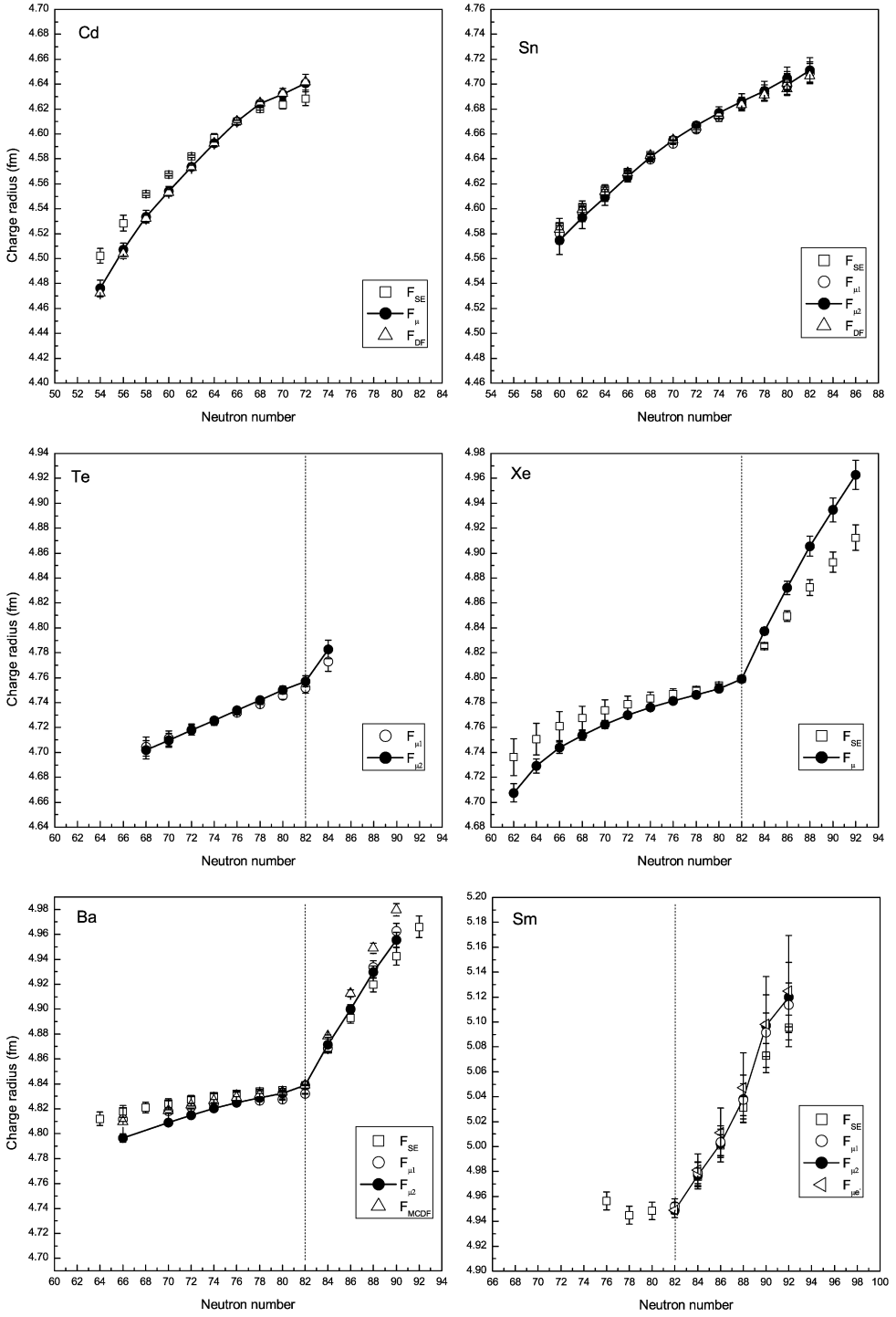

Fig. 1. Experimental charge radius values in the even–even Cd, Sn, Te, Xe, Ba and Sm isotopes (see text).

3. Microscopic evaluation of nuclear charge radii and spectroscopic properties

A systematic investigation of Cd, Sn, Te, Xe, Ba and Sm isotopic chains has been performed on the ground of Hartree–Fock–Bogoliubov solutions deduced under triaxial symmetries from the D1S Gogny effective nucleon–nucleon interaction [30–32]. At first step for each nucleus, constrained HFB (CHFB) solutions are calculated by expansion of single particle states on a triaxial harmonic oscillator basis. Involved numerical methods and codes for this purpose are those described in Ref. [33]. CHFB solutions are mapped against axial $q_0 = \langle \hat{Q}_{20} \rangle$ and triaxial $q_2 = \langle \hat{Q}_{22} \rangle$ components of the mass quadrupole moment. This mapping is as it is usual rewritten in term of polar Bohr's variables:

$$\beta = \frac{\sqrt{5\pi}}{3} \frac{\sqrt{q_0^2 + 3q_2^2}}{A(A^{1/3}\mathrm{r}_0)^2}, \qquad \gamma = \arctan \sqrt{3} \frac{q_2}{q_0} \tag{1}$$

or their usual Cartesian counterparts ($a_0 = \beta \cos\gamma$, $a_2 = \beta \sin\gamma$). In Eq. (1) which connects scaled collective variables (β, γ) with quadrupole moments, the standard liquid drop expression for the mean radius is employed with $\mathrm{r}_0 = 1.2$ fm, A being the particle number.

As known, due to symmetry invariances, this mapping can be restricted to the first sextant $\{0 \leqslant \beta < +\infty; 0 \leqslant \gamma \leqslant \frac{\pi}{3}\}$. In practice, the CHFB calculations are performed on a lattice with typically 80 mesh points in the first sextant with $0 \leqslant \beta \leqslant \beta_c$ using the cutoff value $\beta_c = 0.65$ which will secure, in present case, the evanescent character of collective wave functions (see hereafter).

In each mesh point (β, γ), the neutron $\rho_n^{\beta\gamma}(\vec{r}\,)$ and proton $\rho_p^{\beta\gamma}(\vec{r}\,)$ densities associated with the CHFB solution $\phi^{\beta\gamma}$ give, in particular, the value of neutron and proton point mean square radius by:

$$\langle \mathrm{r}_k^{\beta\gamma} \rangle^2 = \frac{1}{N_k} \int d^3r\, \rho_k^{\beta\gamma}(\vec{r}\,) r^2 \quad \text{with } k = n \text{ or } p \tag{2}$$

where N_p and N_n are the proton and neutron numbers. According to [31] and [34], charge radii are then written in fm units as:

$$\mathrm{r}_c^{\beta\gamma} = \sqrt{\langle \mathrm{r}_p^{\beta\gamma} \rangle^2 + f_{\mathrm{conv}}^{\beta\gamma} + \varepsilon_n} \quad \text{with } f_{\mathrm{conv}}^{\beta\gamma} = \frac{3}{2}\big(B^2 - a\big) \quad \text{and} \quad \varepsilon_n = -0.12 \frac{N_n}{N_p} \big(\mathrm{fm}^2\big). \tag{3}$$

In former expressions, $f_{\mathrm{conv}}^{\beta\gamma}$ carries a proton form factor term ($B = 0.65$ fm) and a correction a due to center of mass motion. This correction, known to be small, is evaluated assuming pure harmonic oscillator wave functions with $a = \hbar/(m\omega_{\beta\gamma} A)$ where m is the nucleonic mass ($\hbar^2/m = 41.47$ MeV fm^2) and where $\omega_{\beta\gamma}$ is the oscillator constant value (in MeV/$\hbar$) chosen in each mesh point to minimize the CHFB energy. Finally, ε_n is a standard expression of the contribution to charge radii associated with the neutron electromagnetic properties.

The HFB state—i.e. the solution $\phi_{\beta_m\gamma_m}$ at the minimum of total energy which arises at deformation $(\beta, \gamma) = (\beta_m, \gamma_m)$—defines what will be called hereafter the "static" properties and, in particular, the charge radius:

$$\mathrm{r}_c^{\mathrm{HFB}} = \mathrm{r}_c^{\beta_m\gamma_m}.$$

At this step, we have applied a configuration mixing approach in the space spanned by the CHFB states $\phi^{\beta\gamma}$ and their rotation transforms. The general frame is the generator coordinate method (GCM) under Gaussian overlap approximation (GOA) for the complete quadrupole collective space i.e. for axial and triaxial quadrupole vibrations together with rotation treated in this

frame on the same footing. Similar approach has been applied to the description of low-energy spectroscopy in various regions of the nuclear chart, and in particular in [35] for light Hg isotopes. Present approach is identical in its principles to those implemented for the description of the normal-super deformation (ND-SD) shape coexistence in mercury-lead and actinide regions [36,37]. Technical details can be found in Ref. [36] and references therein. This approach has been shown to be able to reproduce main trends for low-energy collective levels in deformed and transitional nuclei. However, as well known, the considered collective space is not well adapted to rigid spherical (magic and particularly doubly magic) system, and some evidence of this weakness has thus to be expected in some nuclei of our panel. Here, we will only recall the main steps which are involved in the method.

(i) Under the GOA approximation, the variational GCM Hill–Wheeler equation in the five components of the quadrupole tensor $\{q_{2m}\}$ can be re-written in the intrinsic system under a Schrödinger form i.e. an Hamiltonian $\mathcal{H}^{\text{coll}}$ which takes the form of the so-called full quadrupole collective Bohr Hamiltonian in β, γ, and Euler angles $\Omega = (\theta, \varphi, \psi)$. $\mathcal{H}^{\text{coll}}$ has analytically the same form as the Bohr Hamiltonian considered and numerically solved for the first time in the pioneering work of Ref. [38].

(ii) The Hamiltonian $\mathcal{H}^{\text{coll}}$ involves a kinetic term made with six functions of the deformation, namely the three moments of inertia $\{\mathcal{J}_k(\beta,\gamma)\}_k$ (where k refers to the principal axes ($k = 1$, 2 and 3)) and three mass parameters allowing to built the symmetric vibrational kinetic tensor $\{B_{\alpha\alpha'}(\beta,\gamma)\}_{\alpha,\alpha'=\{\beta,\gamma\}}$ associated with vibrations in β and γ directions and their coupling. These ingredients are calculated for each CHFB solution $\phi^{\beta\gamma}$ using the perturbative approach of motion and linear response theory driving to the so-called Inglis–Belyaev formulas. However, previous works using self-consistent cranking calculations have driven us to introduce a simple but realistic overall scaling factor on $\mathcal{J}_k$ functions to take into account in a simple way the effect of rotation on the nuclear field (the so-called dynamical Thouless–Valatin contribution).

Under GCM–GOA hypotheses, the potential term $V = E^{\text{CHFB}} - E_{\text{zp}}$ of $\mathcal{H}^{\text{coll}}$ carries rotational and vibrational zero point energy contributions which are also evaluated by Inglis–Belyaev cranking series belonging to the linear response theory. Finally, we have used here as it is the case for instance in [36] and [37]:

$$\mathcal{J}_k(\beta,\gamma) = 1.32 * \mathcal{J}_k^{\text{Inglis–Belyaev}}(\beta,\gamma), \quad k = 1,2,3, \tag{4}$$

$$B_{\alpha\alpha'}(\beta,\gamma) = B_{\alpha\alpha'}^{\text{Inglis–Belyaev}}(\beta,\gamma), \quad \alpha,\alpha' = \{\beta,\gamma\}, \tag{5}$$

$$V(\beta,\gamma) = E^{\text{CHFB}}(\beta,\gamma) - E_{\text{zp}}^{\text{Inglis–Belyaev}}(\beta,\gamma). \tag{6}$$

(iii) The Schrödinger equation is solved numerically using expansion techniques similar to those explained in great details in [36]. Deduced eigen energies, $E^{I,n}$ ordered by quantum number n in each block of good angular momentum I, are associated with eigenstates taking the form of normalized combinations:

$$\Psi^{I,n} = \sum_{K\,\text{even}\geqslant 0} A_K^{I,n}(\beta,\gamma)\varphi_{\text{MK}}^I(\Omega) \tag{7}$$

which carries spreading in deformation variables and K-mixing. In Eq. (7), $\varphi_{\text{MK}}^I(\Omega)$ refers to the standard combination (see, e.g. [38]) of Wigner rotation matrices for angular momentum I and its projections $\pm K$ and M on the third axis in intrinsic and laboratory frame, respectively.

Here we focus our interest on properties of the ground states. For this state ($I = K = 0$, $n = 1$), the density of probability in collective space $\rho^{0,1}(\beta,\gamma)$ is given by:

$$\rho^{0,1}(\beta,\gamma) = \left|A_0^{0,1}(\beta,\gamma)\right|^2 \mu(\beta,\gamma) \tag{8}$$

where μ is the metric involving moments of inertia and mass parameters, in such a way that for the normalized state, one has:

$$\int_{\text{sextant}} \rho^{0,1}(\beta,\gamma)\beta\, d\beta\, d\gamma = 1. \tag{9}$$

The associated charge radius, named in what follows "dynamic" or GCM–GOA charge radius writes:

$$\mathrm{r}_c^{\text{GCM–GOA}} = \int_{\text{sextant}} \rho^{0,1}(\beta,\gamma)\mathrm{r}_c^{\beta\gamma}\beta\, d\beta\, d\gamma, \tag{10}$$

where $\mathrm{r}_c^{\beta\gamma}$ is the local CHFB value defined in Eq. (3). Other ground-state properties as $\langle\beta\rangle$ and $\langle\gamma\rangle$ are deduced in the same way through the knowledge of the density $\rho^{0,1}(\beta,\gamma)$.

In the panel of nuclei under study, we can isolate three types of typical behavior in the collective space. Potentials energy surfaces (PES) and deduced densities $\rho^{0,1}$ for rigid or very rigid spherical nuclei are displayed in Fig. 2 for ^{98,130}Cd nuclei taken as examples. Similar information for a soft mid-shell nuclei (^{116}Sn) is shown in Fig. 3, whereas a prolate well-deformed behavior is displayed in Fig. 4 through the ^{126}Ba and ^{154}Sm cases.

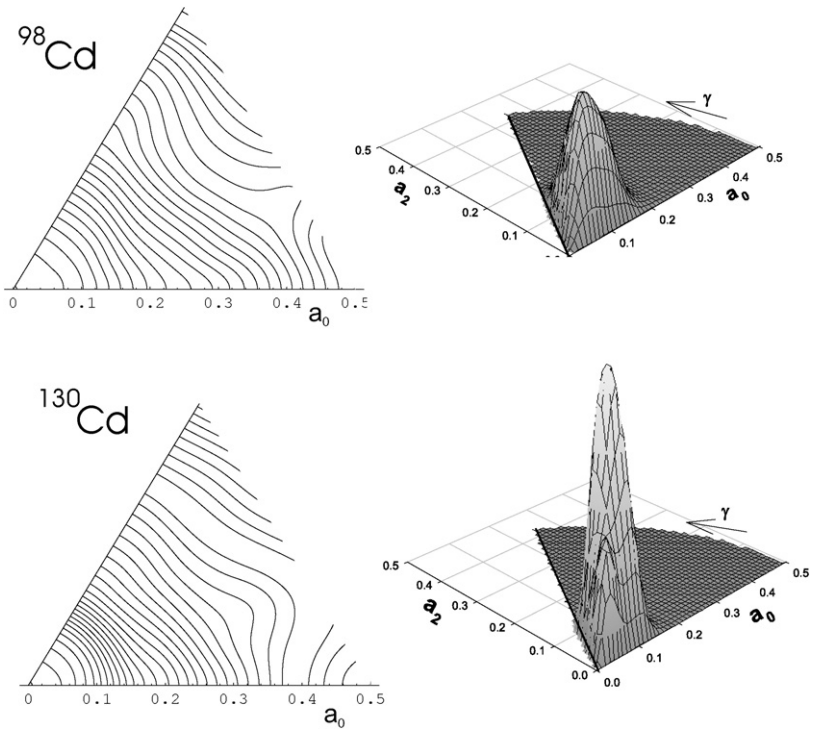

Fig. 2. Potential energy surfaces (left-hand side) and densities of probability in the ground state (right-hand side)—see text—for magic ^{98}Cd ($N = 50$) and ^{130}Cd ($N = 82$) nuclei. Equipotential lines are separated by 1 MeV. Vertical scales for densities $\rho^{0,1}$ are the same for both nuclei. Maximum value of $\rho^{0,1}$ is 116 (respectively 228) for ^{98}Cd (respectively ^{130}Cd).

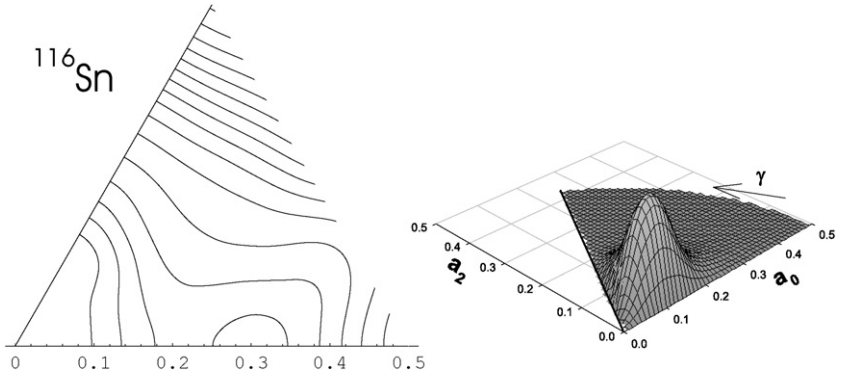

Fig. 3. Same as Fig. 2 for the mid shell nucleus ^{116}Sn ($N = 66$). Vertical scale for potential V and density $\rho^{0,1}$ are the same as in Fig. 2. Maximum value of $\rho^{0,1}$ is 88 for this nucleus.

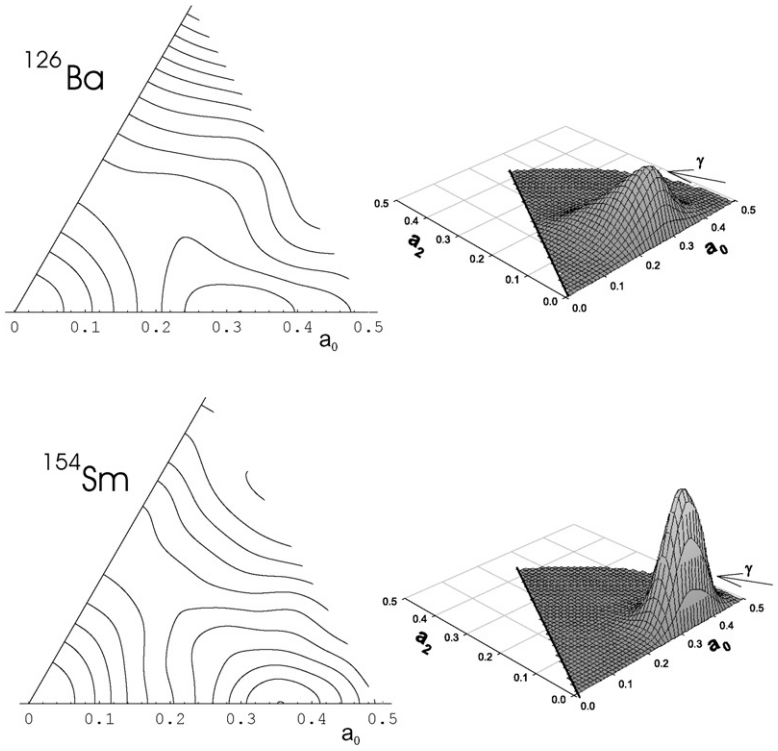

Fig. 4. Same as Fig. 2 for the two prolate well deformed nuclei ^{126}Ba and ^{154}Sm. Vertical scales for potentials V and densities $\rho^{0,1}$ are the same as in Fig. 2. Maximum value of $\rho^{0,1}$ is 65 (respectively 136) for ^{126}Ba (respectively ^{154}Sm).

Hereafter and in the discussion of Section 4, we will also refer to reduced E2 transition probability values calculated for the first transition in the ground state (gs) band, namely $0^+_{\rm gs} \to 2^+_{\rm gs}$. These calculations have been performed under simple hypothesis of uniform charge distribution in collective model following [38]. That is known to be quite reliable as long as a shape transition does not occur between the initial and the final states. Qualitatively, one can retain that

the microscopic charge quadrupole operator, which is non-local in the present collective space, can be replaced by the corresponding local collective model operator as long as densities in the initial and final states are high in the same area of the collective space. This is clearly the case for nuclei under study, and, in particular for the transition $0^+_{\rm gs} \to 2^+_{\rm gs}$.

To be more explicit on this point, collective model assumption of Ref. [38], means that the considered charge quadrupole operator acting in the collective space is taken simply as the two component operator:

$$\hat{Q}_0 = \frac{3}{4\pi} Z\big(\mathrm{r}_0 A^{1/3}\big)^2 \beta \cos\gamma, \qquad \hat{Q}_{2'} = \frac{3}{4\pi} Z\big(\mathrm{r}_0 A^{1/3}\big)^2 \beta \sin\gamma \tag{11}$$

with $\mathrm{r}_0 = 1.2$ fm.

Under these hypotheses, the reduced E2 transition probability between an initial (I, n) and a final (I', n') state of our spectrum, writes:

$$B\big(\mathrm{E2};\,(I,n) \to (I',n')\big) = \frac{1}{(2I+1)} \big|\langle I, n \| \mathcal{M}(\mathrm{E2}) \| I' n' \rangle\big|^2, \tag{12}$$

where the reduced matrix element, for transitions $(0, n) \to (2, n')$ under present scope writes after evaluating geometrical coefficients:

$$\langle 0, n \| \mathcal{M}(E2) \| 2, n' \rangle = \big\langle A_0^{0,n} \big| \hat{Q}_0 \big| A_0^{2,n'} \big\rangle + \big\langle A_0^{0,n} \big| \hat{Q}_{2'} \big| A_2^{2,n'} \big\rangle \tag{13}$$

with

$$\big\langle A_K^{I,n} \big| \hat{Q}_m \big| A_{K'}^{I',n'} \big\rangle = \int\limits_{\text{sextant}} A_K^{I,n}(\beta,\gamma)\, \hat{Q}_m\, A_{K'}^{I,n'}(\beta,\gamma) \mu(\beta,\gamma) \beta \, d\beta \, d\gamma. \tag{14}$$

This paper is focused on measurement and evaluation of charge radii. To control the validity of the present GCM–GOA approach, it is however of some interest to see some results obtained in this frame for other observables as excitation energy of first levels in the ground state band $(2^+_{\rm gs}, 4^+_{\rm gs})$ and these E2 transition rates $(0^+_{\rm gs} \to 2^+_{\rm gs})$ discussed above. For all isotopic chains under study, these results are drawn in Fig. 5. The main trends are satisfactorily reproduced for these quantities. Main discrepancies appear for magic and doubly magic nuclei. The only case where the $B(\mathrm{E2})$ is over-evaluated do correspond to the magic $N = 50$ Sn nuclei. This overestimation of the collectivity corresponds to a certain inadequation of the considered space as already mentioned. The very strong effect on excitation energies due to the $N = 82$ shell closure is often missed by the calculation. It should be noticed, however, that such approaches under quasiparticle hypothesis, manage with a spreading in the number of particles. It could not be very surprising to see a smoothing on excitation energies as function of N in the vicinity of the violent $N = 82$ shell closure. The phenomenon is strong and makes the systems with $N \pm 2$ quite different from the system with N neutrons. Keeping in mind that we have to take care around shell and doubly shell closures, the overall agreement with experimental data which has been shown demonstrates that the present theoretical description provides reliable gs wave functions and therefore a convenient ground to study in more detail the question of charge radii.

4. Discussion

The static and dynamic root mean square charge radii calculated within the theoretical approach described above are displayed in Fig. 6. Following the analysis of Section 2, they are

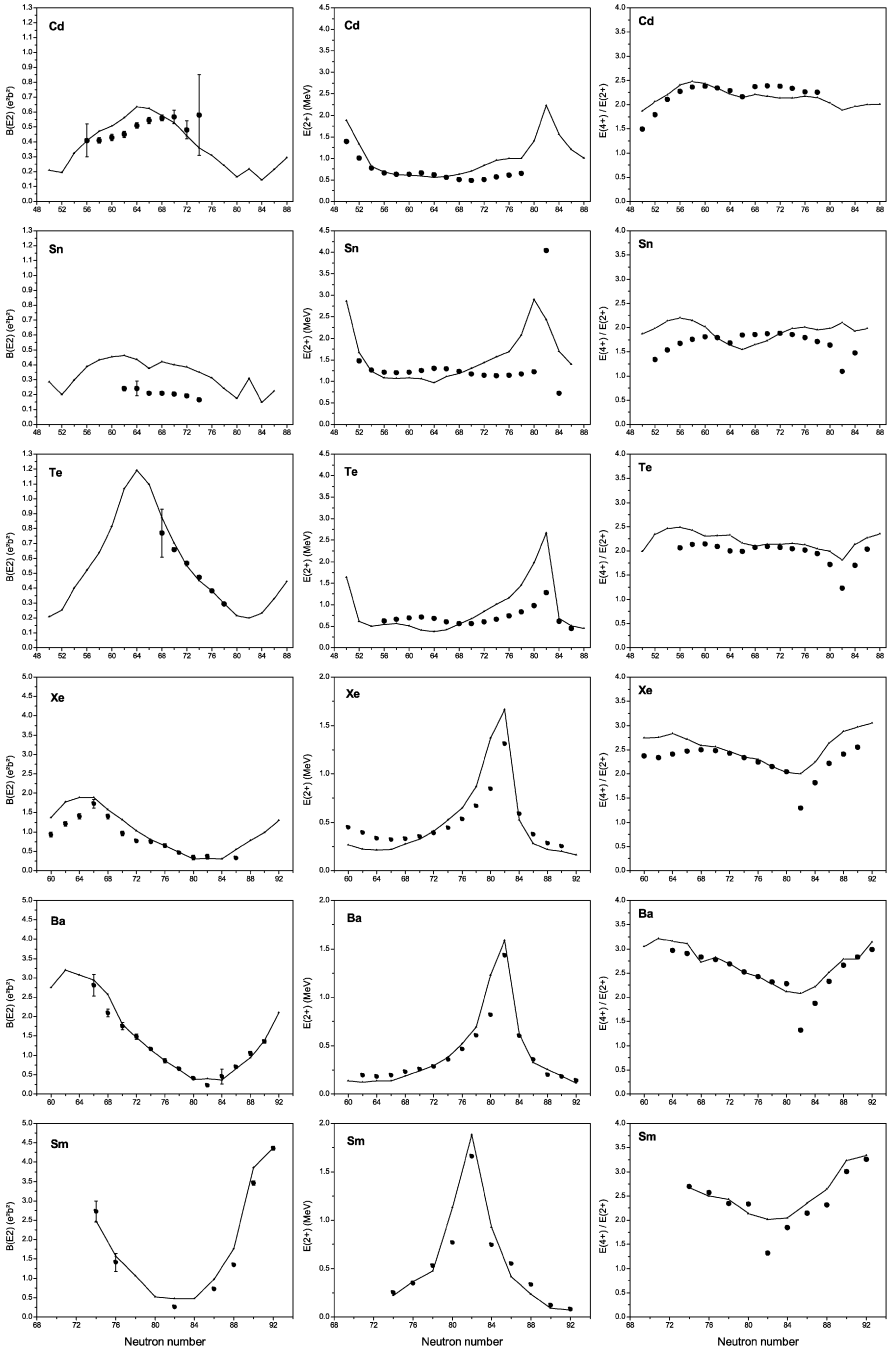

Fig. 5. GCM–GOA calculated quantities (full lines and triangles) are compared with experimental values (full dots with error bars for B(E2) values) in each isotopic chain from successively Cd (upper part), Sn, Te, Xe, Ba to Sm (lower part). This comparison is displayed for transition probabilities $B(\mathrm{E2}; 0^+_{\mathrm{gs}} \to 2^+_{\mathrm{gs}})$ (left column), excitation energy $\mathrm{E}(2^+_{\mathrm{gs}})$ of the first excited state (central column) and the ratio of excitation energies $\mathrm{E}(4^+_{\mathrm{gs}})/\mathrm{E}(2^+_{\mathrm{gs}})$ as a measurement of the vibrational–rotational character of the spectrum. The experimental data have been taken from Refs. [39,40].

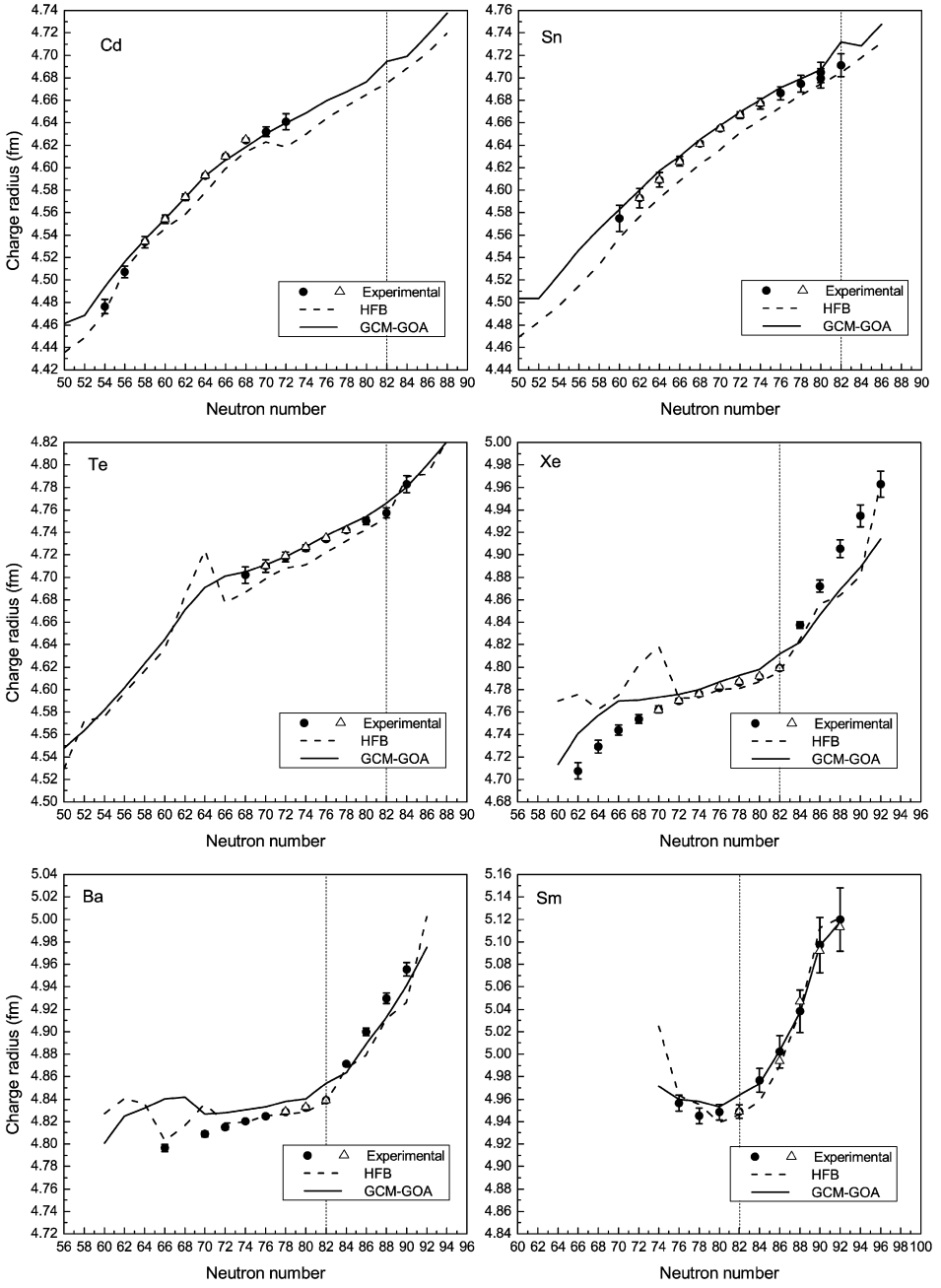

Fig. 6. Experimental and calculated charge radii in even–even Cd, Sn, Te, Xe, Ba and Sm isotopes. The experimental r_c values given in Ref. [1] for even–even nuclei are shown as open triangles.

compared in this figure with the r_c values we deduced from the optical isotope shift measurements by a King plot analysis performed using the r_c values known for the stable isotopes either from muonic atom experiments or from a combined analysis.

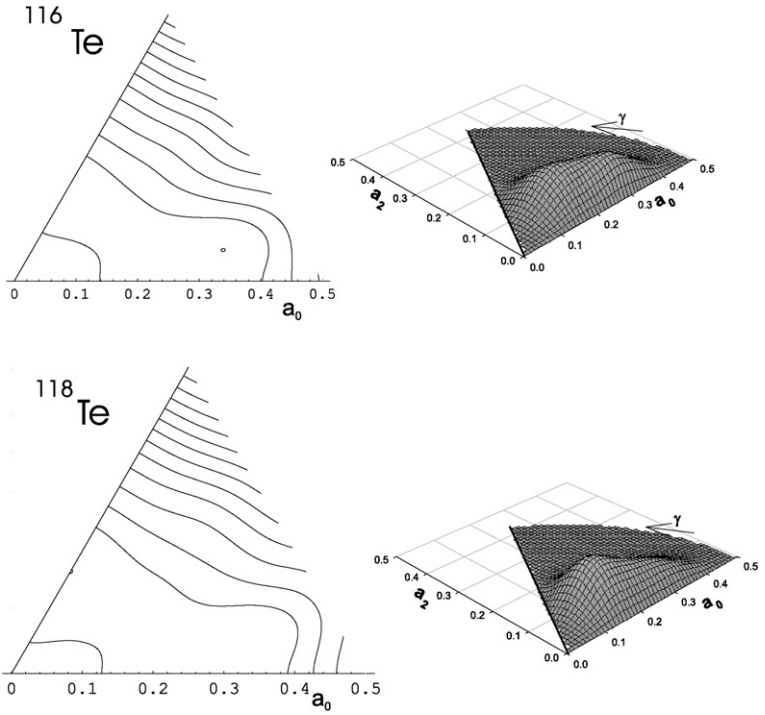

Fig. 7. Same as Fig. 2 for $^{116-118}$Te. Vertical scales for potentials V and densities $\rho^{0,1}$ are the same as in Fig. 2. Maximum value of $\rho^{0,1}$ is 38 (respectively 45) for ^{116}Te (respectively ^{118}Te).

For the Cd, Sn, Te and Sm isotopic series, we must note that the best agreement is clearly obtained between the experimental data and the dynamic theoretical predictions. However for the nuclei having a neutron number very close to a magic one ($N = 50$ or 82), the agreement can become better with the static calculations; this is the case for the doubly magic ^{132}Sn, magic ^{134}Te, Cd with $N < 58$ and Sm with $76 < N < 84$.

On the other hand, for the Xe and Ba isotopic series, some of the r_c values are rather in best agreement with these given by the static predictions whereas the curves have a smooth behaviour similar to this predicted by the dynamic calculations. One can note, in particular, that the jumps found in the r_c static curves never exist in the experimental ones. The jumps happen close to the neutron mid-shell $N = 66$; namely between $N = 64$ and 66 for the Te nuclei and between $N = 70$ and 72 for the Xe and Ba ones. The potential energy surfaces and the corresponding densities of ^{116,118}Te ($N = 64$ and $N = 66$) and ^{124,126}Xe ($N = 70$ and $N = 72$) are shown in Figs. 7 and 8. These potential energy surfaces are smooth with a very large γ valley and without any deep well, which clearly indicates that the four nuclei are γ-soft. In such a case, the HFB solution localized at the minimum is a poor description of the system which strongly spreads out on the deformation space. This means that the deduced static deformation is then not valuable. For example, the potential energy surfaces of ^{116}Te and ^{118}Te are very similar but a small minimum is visible at $\beta = 0.35$ for ^{116}Te whereas no minimum appears for ^{118}Te. This very small difference could explain the static r_c curve jump that is found between ^{116}Te and ^{118}Te because of the obvious strong influence of the deformation on the r_c value. The static and dynamic deformation parameters are shown in Fig. 9. We can see that the static deformation

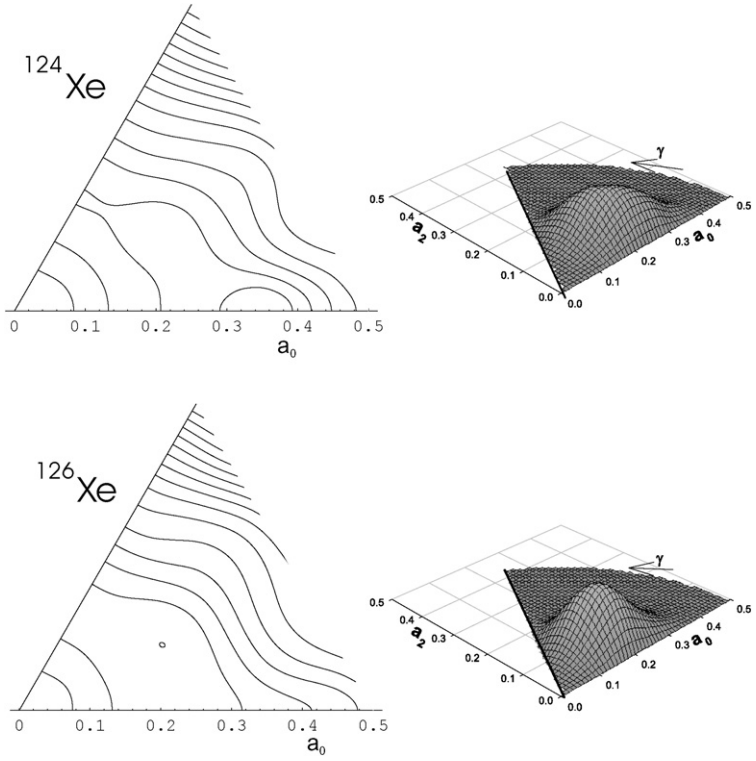

Fig. 8. Same as Fig. 2 for $^{124-126}$Xe. Vertical scales in potentials V and densities $\rho^{0,1}$ are the same as in Fig. 2. Maximum value of $\rho^{0,1}$ is 46 (respectively 59) for ^{124}Xe (respectively ^{126}Xe).

parameter $\beta = 0.35$ for ^{116}Te is large while it is only $\beta = 0.17$ for ^{118}Te. In the same way the static r_c curve jumps calculated at $N = 70$ for the Xe and Ba isotopic series are due to sudden changes of the deformation parameters (see Fig. 9). We can conclude that the local irregularities found for the r_c curves with the static calculations are artefacts that can come out for a soft nucleus for which the potential energy surface is very smooth.

Such artefacts do not exist in dynamic calculations since the density is determined taking into account the shape of the whole potential energy surface. Thus, for example, the densities calculated for ^{116}Te and ^{118}Te are very similar, they spread out on a large part of the collective space, from $\beta = 0.1$ to 0.4. In such cases, good predictions can only be obtained by use of dynamical calculations, taking into account long range correlations. So, except for nuclei situated very close to the magic numbers, the dynamic approach is expected to provide the best description.

Now, it remains to understand why the static r_c values seem to be in a better agreement with the experimental r_c values than the dynamic ones for the Xe and Ba isotopic series. Is this due to the calculation quality or to the experimental determination? To seek to answer the first question, it is possible to estimate the calculation quality by having a look again at the Fig. 5 where some other experimental and predicted spectroscopic properties ($B(E2)$, $E(2+)$, $E(4+)/E(2+)$) are compared. The agreement between predicted and experimental results is at least as good for the Xe and Ba isotopic series as for the other ones. The agreement is even particularly excellent for the Ba nuclei. The calculation quality does not seem, hence, to be called in question for Xe and Ba nuclei. As for the second question, we have to remind that the larger difference between

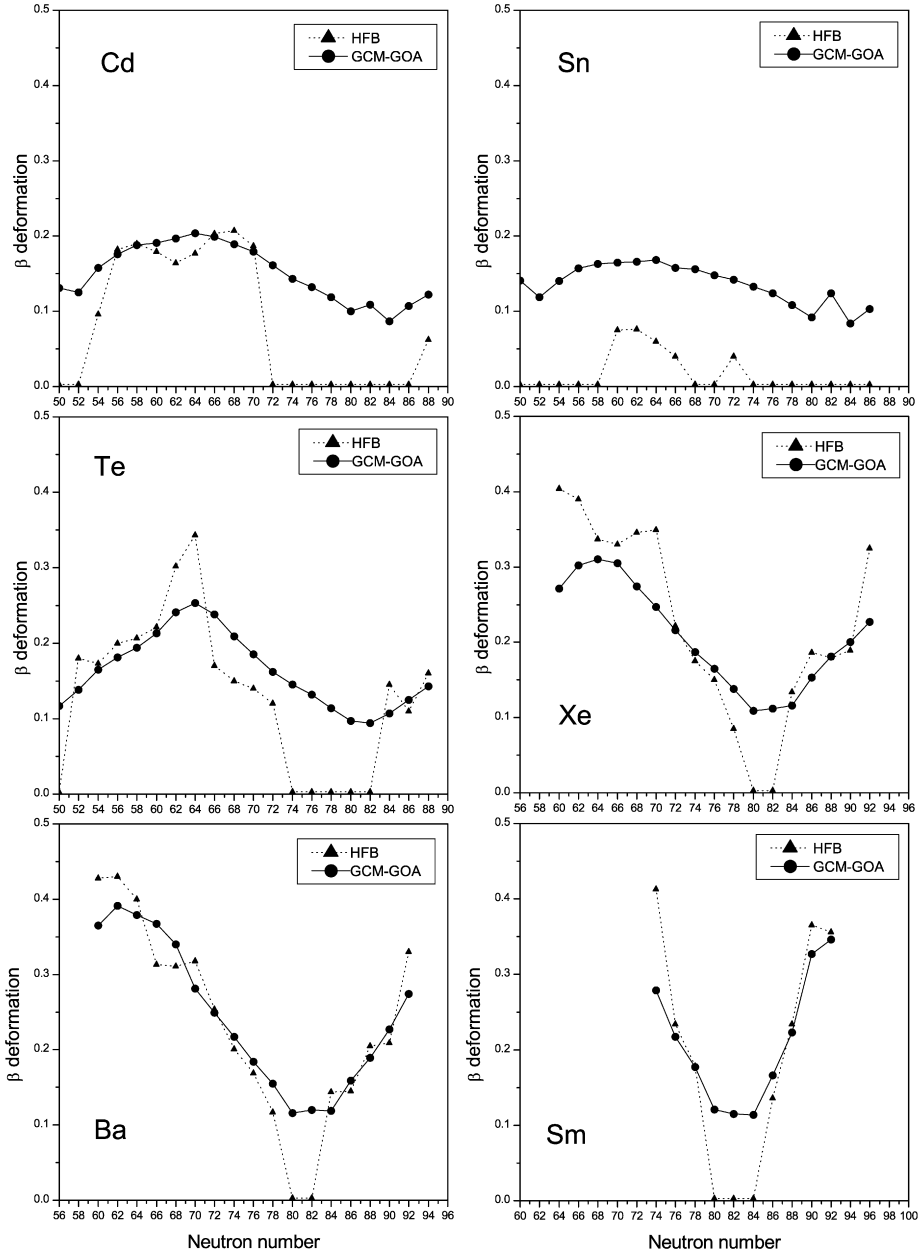

Fig. 9. Theoretical (HFB and GCM–GOA) deformation parameter β for the ground state against the neutron number N in even–even Cd, Sn, Te, Xe, Ba and Sm isotopes.

the various experimental determinations has been obtained for the Xe and Ba isotopic series (see Fig. 1). Moreover, some reasons of uncertainty in the r_c determination in the Xe isotopic series have been stressed in Section 2. So, for Xe and Ba nuclei, we compare in Fig. 10 the r_c values obtained with dynamic calculations with the two sets of data given by the semi-empirical

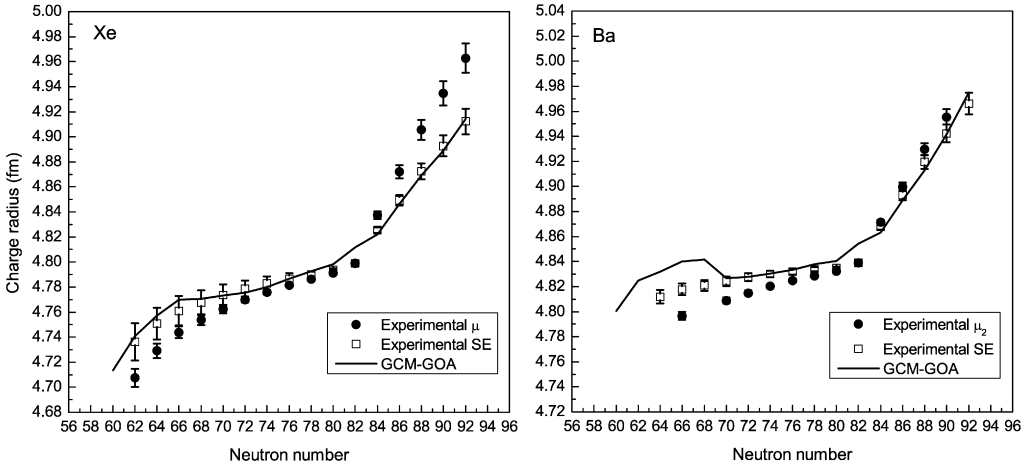

Fig. 10. For Xe (left-hand side) and Ba (right-hand side) nuclei, charge radii deduced from semi-empirical method (open squares) and with the King plot on the ground of muonic atom results (full dots) are compared with dynamical charge radii provided by the GCM–GOA approach (full line).

method (F_{SE}) and the King plot determination ($F_{\mu 2}$) using the muonic atom results. The best agreement is obviously obtained with the data set semi-empirically determined. It is worth noting that the muonic r_c values of the stable isotopes (reported as open triangle in Fig. 6) used to perform the King plot analysis, are all located close to the magic neutron number $N = 82$ where the r_c values are almost constant and consequently where the mean square charge radius changes are very small. In these particular conditions the F value can be not enough precisely determined to get the right r_c values for the nuclei located far away from the magic number. Moreover, the muonic r_c values reported in the Fricke table (Ref. [1]) for the stable Xe and Ba nuclei have been corrected for nuclear polarization effects assuming a spherical nuclear shape whereas for the lightest isotopes a deformation already exists. This approximation could also contribute to increase the uncertainty on the F value. All of these facts show the limit of the method. For these critical cases it is very clear that a combined analysis as that used for the Sm nuclei, is absolutely necessary to get valuable results to be compared with theoretical predictions.

5. Conclusion

In this work, the r_c values along the Cd, Sn, Te, Xe, Ba and Sm isotopic series have been obtained using mainly the muonic atom and optical spectroscopy results. Among the various methods employed to determine the electronic factor F and the Specific over Normal mass shift S/N, the King plot analysis using the r_c values extracted for the stable isotopes from muonic atom experiments leads as expected to the most accurate r_c values. However, this method seems to reach its limits in cases where the reference stable isotopes are close to a magic number and drive therefore a low slope of the r_c curve as function of the neutron number. This has been shown in Xe and Ba isotopic chains. In such cases, a combined analysis would be essential but is unfortunately unavailable up to now.

The excellent agreement found between the experimental data and dynamical GCM–GOA calculations for Cd Sn Te isotopes has shown that a theoretical approach must take into account

long range correlations especially for γ-soft and weakly deformed nuclei. Of course in cases of well deformed nuclei, as Sm, the static and dynamic deformations are similar and lead to almost the same r_c values. In all the isotopic series under study, the low-energy spectroscopy is well reproduced by GCM–GOA calculations. In particular, this is the case for the Xe and Ba chains. In these nuclei, the GCM–GOA r_c values are thus expected to be also in good agreement with the experimental values. The fact that the dynamical charge radii are in better agreement with the experimental r_c values obtained using the semi-empirical F_{SE} factor than with those calculated using the muonic F_μ factor supports the limitation of the F_μ determinations evocated above for the Xe and Ba nuclei.

Appendix A

Table 1
Charge radii (in fm) for Cd isotopes

A	N	F_{SE}[a]	F_μ[b]	F_{DF}[c]	HFB	GCM–GOA
98	50				4.4354	4.4614
100	52				4.4487	4.4684
102	54	4.5022 ± 0.0058	4.4763 ± 0.0063	4.4724 ± 0.0031	4.4709	4.4939
103	55	4.5140 ± 0.0056	4.4904 ± 0.0057	4.4869 ± 0.0031		
104	56	4.5285 ± 0.0062	4.5071 ± 0.0053	4.5040 ± 0.0039	4.5091	4.5162
105	57	4.5364 ± 0.0048	4.5174 ± 0.0046	4.5147 ± 0.0030		
106	58	4.5517 ± 0.0010	4.5337 ± 0.0050	4.5324 ± 0.0026	4.5308	4.5362
107	59	4.5575 ± 0.0042	4.5428 ± 0.0037	4.5409 ± 0.0029		
108	60	4.5673 ± 0.0010	4.5541 ± 0.0039	4.5531 ± 0.0022	4.5457	4.5545
109	61	4.5689 ± 0.0054	4.5585 ± 0.0030	4.5575 ± 0.0044		
110	62	4.5822 ± 0.0010	4.5736 ± 0.0029	4.5730 ± 0.0018	4.5587	4.5735
111	63	4.5845 ± 0.0010	4.5776 ± 0.0103	4.5778 ± 0.0016		
111m	63	4.5832 ± 0.0119	4.5784 ± 0.0025	4.5767 ± 0.0111		
112	64	4.5969 ± 0.0034	4.5926 ± 0.0019	4.5924 ± 0.0029	4.5777	4.5929
113	65	4.5993 ± 0.0010	4.5954 ± 0.0076	4.5972 ± 0.0012		
113m	65	4.5991 ± 0.0084	4.5975 ± 0.0016	4.5950 ± 0.0083		
114	66	4.6100 ± 0.0010	4.6100 ± 0.0010	4.6100 ± 0.0010	4.5991	4.6066
115	67	4.6125 ± 0.0059	4.6148 ± 0.0058	4.6149 ± 0.0060		
115m	67	4.6133 ± 0.0023	4.6148 ± 0.0025	4.6156 ± 0.0024		
116	68	4.6202 ± 0.0010	4.6245 ± 0.0018	4.6246 ± 0.0014	4.6141	4.6184
118	70	4.6235 ± 0.0034	4.6320 ± 0.0044	4.6325 ± 0.0040	4.623	4.6305
120	72	4.6283 ± 0.0055	4.6408 ± 0.0070	4.6416 ± 0.0064	4.6182	4.6397
122	74				4.6301	4.6489
124	76				4.6438	4.6595
126	78				4.6548	4.6675
128	80				4.6652	4.6766
130	82				4.6751	4.6945
132	84				4.6887	4.6991
134	86				4.702	4.7178
136	88				4.7199	4.7372

[a] $\delta\langle r_c^2\rangle$ values from Ref. [6] and r_c (^{114}Cd) from Ref. [1]. [b] $F = -4.37 \pm 0.18$ GHz/fm^2, $S/N = 2.43 \pm 0.35$, $k = 0.977$ (see text), IS taken from Ref. [12] and r_c (^{114}Cd) from Ref. [1]. [c] F from Dirac–Fock calculations [10,12], $S/N = 2.15 \pm 0.18$, $k = 0.977$ (see text), IS taken from Ref. [12] and r_c (^{114}Cd) from Ref. [1].

Table 2
Charge radii (in fm) for Sn isotopes

A	N	F_{SE}[a]	$F_{\mu 1}$[b]	$F_{\mu 2}$[c]	F_{DF}[d]	HFB	GCM–GOA
100	50					4.469	4.5033
102	52					4.4823	4.5034
104	54					4.497	4.5248
106	56					4.5147	4.5467
108	58					4.5337	4.5653
110	60	4.5860 ± 0.0028	4.5801 ± 0.0083	4.5748 ± 0.0115	4.5833 ± 0.0088	4.5574	4.5828
111	61	4.5916 ± 0.0027	4.5860 ± 0.0074	4.5804 ± 0.0102	4.5884 ± 0.0082		
112	62	4.6013 ± 0.0022	4.5961 ± 0.0064	4.5928 ± 0.0087	4.5993 ± 0.0070	4.5763	4.6001
113	63	4.6077 ± 0.0021	4.6028 ± 0.0059	4.5999 ± 0.0081	4.6057 ± 0.0062		
114	64	4.6154 ± 0.0018	4.6108 ± 0.0048	4.6091 ± 0.0065	4.6139 ± 0.0053	4.5928	4.6171
115	65	4.6203 ± 0.0017	4.6160 ± 0.0042	4.6138 ± 0.0057	4.6183 ± 0.0048		
116	66	4.6295 ± 0.0014	4.6256 ± 0.0032	4.6257 ± 0.0042	4.6287 ± 0.0037	4.6084	4.6301
117	67	4.6347 ± 0.0012	4.6310 ± 0.0026	4.6309 ± 0.0034	4.6335 ± 0.0031		
117m	67	4.6343 ± 0.0013	4.6306 ± 0.0028	4.6303 ± 0.0038	4.6330 ± 0.0031		
118	68	4.6429 ± 0.0010	4.6396 ± 0.0017	4.6413 ± 0.0021	4.6427 ± 0.0021	4.6229	4.6451
119	69	4.6475 ± 0.0008	4.6444 ± 0.0012	4.6458 ± 0.0015	4.6468 ± 0.0017		
120	70	4.6550 ± 0.0006	4.6522 ± 0.0006	4.6550 ± 0.0006	4.6550 ± 0.0006	4.6362	4.6573
121	71	4.6595 ± 0.0008	4.6570 ± 0.0013	4.6594 ± 0.0015	4.6591 ± 0.0011		
121m	71	4.6589 ± 0.0008	4.6563 ± 0.0012	4.6584 ± 0.0014	4.6583 ± 0.0010		
122	72	4.6658 ± 0.0010	4.6635 ± 0.0023	4.6668 ± 0.0031	4.6657 ± 0.0020	4.651	4.6693
123	73	4.6694 ± 0.0012	4.6673 ± 0.0025	4.6696 ± 0.0032	4.6685 ± 0.0021		
124	74	4.6755 ± 0.0013	4.6737 ± 0.0035	4.6770 ± 0.0047	4.6751 ± 0.0030	4.6622	4.6805
125	75	4.6791 ± 0.0016	4.6774 ± 0.0038	4.6798 ± 0.0052	4.6779 ± 0.0032		
125m	75	4.6775 ± 0.0040	4.6758 ± 0.0037	4.6773 ± 0.0049	4.6757 ± 0.0030		
126	76	4.6846 ± 0.0051	4.6832 ± 0.0045	4.6862 ± 0.0060	4.6836 ± 0.0039	4.6736	4.6911
127	77	4.6878 ± 0.0056	4.6866 ± 0.0050	4.6888 ± 0.0067	4.6862 ± 0.0041		
127m	77	4.6858 ± 0.0053	4.6845 ± 0.0049	4.6854 ± 0.0065	4.6833 ± 0.0038		
128	78	4.6930 ± 0.0063	4.6920 ± 0.0056	4.6946 ± 0.0076	4.6914 ± 0.0047	4.6844	4.6992
129	79	4.6941 ± 0.0065	4.6933 ± 0.0060	4.6938 ± 0.0080	4.6911 ± 0.0047		
129m	79	4.6969 ± 0.0069	4.6962 ± 0.0061	4.6984 ± 0.0081	4.6950 ± 0.0051		
130	80	4.7023 ± 0.0077	4.7018 ± 0.0067	4.7047 ± 0.0090	4.7006 ± 0.0057	4.6946	4.7072
130m	80	4.6991 ± 0.0073	4.6985 ± 0.0065	4.6994 ± 0.0086	4.6962 ± 0.0052		
131	81	4.7080 ± 0.0086	4.7077 ± 0.0073	4.7115 ± 0.0100	4.7067 ± 0.0064		
131m	81	4.7108 ± 0.0090	4.7105 ± 0.0074	4.7161 ± 0.0102	4.7105 ± 0.0068		
132	82	4.7093 ± 0.0088	4.7091 ± 0.0075	4.7111 ± 0.0101	4.7067 ± 0.0064	4.7043	4.7318
134	84					4.7179	4.7285
136	86					4.7311	4.7476

[a] F, SMS and k from Ref. [13], IS from Refs. [5,13] and r_c (^{120}Sn) from Ref. [1]. [b] F, S/N and k from Ref. [5], IS from Refs. [5,13] and r_c (^{120}Sn) from Ref. [15]. [c] $F = 2.04 \pm 0.2$ GHz/fm^2, $S/N = -0.78 \pm 0.32$ and $k = 0.975$ (see text), IS from Refs. [5,13] and r_c (^{120}Sn) from Ref. [1]. [d] F from Dirac–Fock calculations, S/N and k from Ref. [16], IS from Refs. [5,13] and r_c (^{120}Sn) from Ref. [1].

Table 3
Charge radii (in fm) for Te isotopes

A	N	$F_{\mu 1}$[a]	$F_{\mu 2}$[b]	HFB	GCM–GOA
102	50			4.5293	4.5476
104	52			4.5716	4.5634
106	54			4.576	4.5818

Table 3 (*continued*)

A	N	$F_{\mu 1}$ [a]	$F_{\mu 2}$ [b]	HFB	GCM–GOA
108	56			4.597	4.6014
112	60			4.6358	4.6445
114	62			4.6838	4.6709
116	64			4.7234	4.6908
118	66			4.6777	4.701
120	68	4.7046 ± 0.0076	4.7020 ± 0.0073	4.6865	4.7048
122	70	4.7112 ± 0.0060	4.7098 ± 0.0056	4.6985	4.7111
123	71	4.7127 ± 0.0056	4.7114 ± 0.0051		
124	72	4.7183 ± 0.0045	4.7180 ± 0.0042	4.7082	4.7182
125	73	4.7201 ± 0.0041	4.7200 ± 0.0036		
126	74	4.7250 ± 0.0031	4.7258 ± 0.0028	4.7109	4.7272
128	76	4.7319 ± 0.0018	4.7339 ± 0.0016	4.722	4.7371
130	78	4.7388 ± 0.0005	4.7420 ± 0.0005	4.7326	4.7455
132	80	4.7456 ± 0.0029	4.7500 ± 0.0033	4.7428	4.7539
134	82	4.7517 ± 0.0041	4.7571 ± 0.0045	4.7525	4.7659
136	84	4.7729 ± 0.0077	4.7828 ± 0.0075	4.7897	4.7803

[a] $F = 4.66 \pm 0.86$ GHz/fm^2, $S/N = -1.89 \pm 0.33$ and $k = 0.974$ (see text), IS from Refs. [17,18] and r_c (^{130}Te) from Ref. [19]. [b] $F = 3.78 \pm 0.48$ GHz/fm^2, $S/N = -1.73 \pm 0.37$ and $k = 0.974$ (see text), IS from Refs. [17,18] and r_c (^{130}Te) from Ref. [1].

Table 4
Charge radii (in fm) for Xe isotopes

A	N	F_{SE} [a]	F_{μ} [b]	HFB	GCM–GOA
114	60			4.7697	4.7136
116	62	4.7362 ± 0.0149	4.7075 ± 0.0073	4.7759	4.7408
118	64	4.7508 ± 0.0127	4.7291 ± 0.0057	4.7622	4.7571
120	66	4.7610 ± 0.0117	4.7439 ± 0.0046	4.775	4.7698
122	68	4.7677 ± 0.0095	4.7537 ± 0.0039	4.8016	4.7707
124	70	4.7737 ± 0.0085	4.7624 ± 0.0032	4.8187	4.7733
126	72	4.7788 ± 0.0064	4.7699 ± 0.0023	4.7724	4.7756
128	74	4.7831 ± 0.0053	4.7760 ± 0.0019	4.7729	4.7799
129	75	4.7831 ± 0.0043	4.7760 ± 0.0019		
130	76	4.7868 ± 0.0043	4.7813 ± 0.0015	4.7798	4.7867
131	77	4.7861 ± 0.0032	4.7802 ± 0.0015		
132	78	4.7902 ± 0.0022	4.7863 ± 0.0011	4.7812	4.7926
134	80	4.7936 ± 0.0014	4.7911 ± 0.0007	4.7869	4.7981
136	82	4.7990 ± 0.0001	4.7990 ± 0.0001	4.7961	4.8117
137	83	4.8099 ± 0.0011	4.8149 ± 0.0014		
138	84	4.8254 ± 0.0022	4.8373 ± 0.0029	4.8247	4.8221
139	85	4.8363 ± 0.0032	4.8531 ± 0.0041		
140	86	4.8494 ± 0.0042	4.8721 ± 0.0053	4.8561	4.8464
141	87	4.8602 ± 0.0052	4.8878 ± 0.0065		
142	88	4.8724 ± 0.0063	4.9055 ± 0.0079	4.8637	4.869
143	89	4.8810 ± 0.0073	4.9178 ± 0.0085		
144	90	4.8927 ± 0.0083	4.9346 ± 0.0097	4.8814	4.889
146	92	4.9123 ± 0.0103	4.9628 ± 0.0117	4.9634	4.9141

[a] $\delta\langle r_c^2 \rangle$ from Ref. [20] and r_c (^{136}Xe) from Ref. [1]. [b] $F = -1.56 \pm 0.11$ GHz/fm^2, $S/N = 0.192 \pm 0.266$ and $k = 0.972$ (see text), IS from Ref. [20] and r_c (^{136}Xe) from Ref. [1].

Table 5
Charge radii (in fm) for Ba isotopes

A	N	F_{SE}[a]	$F_{\mu 1}$[b]	$F_{\mu 2}$[c]	F_{MCDF}[d]	HFB	GCM–GOA
116	60					4.8272	4.8007
118	62					4.8405	4.8249
120	64	4.8119 ± 0.0053				4.8359	4.832
121	65	4.8200 ± 0.0051					
122	66	4.8179 ± 0.0048	4.8116 ± 0.0016	4.7966 ± 0.0032	4.8095 ± 0.0110	4.8031	4.8402
123	67	4.8162 ± 0.0046	4.8090 ± 0.0016	4.7963 ± 0.0031	4.8073 ± 0.0101		
124	68	4.8209 ± 0.0043				4.8165	4.8417
125	69	4.8202 ± 0.0040	4.8132 ± 0.0015	4.8033 ± 0.0027	4.8128 ± 0.0087		
126	70	4.8243 ± 0.0038	4.8180 ± 0.0014	4.8089 ± 0.0025	4.8184 ± 0.0082	4.8361	4.8266
127	71	4.8226 ± 0.0035	4.8154 ± 0.0013	4.8085 ± 0.0023	4.8163 ± 0.0073		
128	72	4.8275 ± 0.0032	4.8212 ± 0.0012	4.8149 ± 0.0021	4.8228 ± 0.0068	4.8184	4.8277
129	73	4.8268 ± 0.0030	4.8200 ± 0.0011	4.8155 ± 0.0020	4.8221 ± 0.0061		
129m	73	4.8255 ± 0.0030	4.8183 ± 0.0012	4.8141 ± 0.0021	4.8203 ± 0.0061		
130	74	4.8301 ± 0.0027	4.8237 ± 0.0010	4.8202 ± 0.0017	4.8265 ± 0.0054	4.8194	4.8304
131	75	4.8294 ± 0.0025	4.8225 ± 0.0010	4.8208 ± 0.0016	4.8257 ± 0.0047		
131m	75	4.8291 ± 0.0025	4.8220 ± 0.0010	4.8204 ± 0.0016	4.8252 ± 0.0047		
132	76	4.8320 ± 0.0022	4.8254 ± 0.0009	4.8247 ± 0.0014	4.8292 ± 0.0041	4.825	4.8332
133	77	4.8303 ± 0.0020	4.8228 ± 0.0009	4.8241 ± 0.0013	4.8270 ± 0.0035		
133m	77	4.8316 ± 0.0020	4.8244 ± 0.0008	4.8254 ± 0.0013	4.8287 ± 0.0034		
134	78	4.8339 ± 0.0017	4.8265 ± 0.0007	4.8287 ± 0.0011	4.8314 ± 0.0028	4.8265	4.8378
135	79	4.8313 ± 0.0016	4.8227 ± 0.0009	4.8271 ± 0.0011	4.8279 ± 0.0022		
135m	79	4.8335 ± 0.0014	4.8261 ± 0.0007	4.8298 ± 0.0010	4.8314 ± 0.0022		
136	80	4.8350 ± 0.0011	4.8273 ± 0.0006	4.8323 ± 0.0008	4.8332 ± 0.0016	4.8285	4.8403
137	81	4.8331 ± 0.0009	4.8246 ± 0.0007	4.8316 ± 0.0008	4.8307 ± 0.0010		
137m	82	4.8394 ± 0.0004	4.8329 ± 0.0004	4.8383 ± 0.0005	4.8395 ± 0.0009		
138	82	4.8390 ± 0.0004	4.8320 ± 0.0004	4.8390 ± 0.0004	4.8390 ± 0.0004	4.8373	4.8541
139	83	4.8517 ± 0.0012	4.8481 ± 0.0012	4.8534 ± 0.0011	4.8564 ± 0.0011		
140	84	4.8676 ± 0.0022	4.8684 ± 0.0021	4.8713 ± 0.0020	4.8782 ± 0.0017	4.8674	4.8634
141	85	4.8792 ± 0.0030	4.8829 ± 0.0027	4.8845 ± 0.0026	4.8940 ± 0.0023		
142	86	4.8929 ± 0.0041	4.9002 ± 0.0035	4.8998 ± 0.0034	4.9126 ± 0.0028	4.8792	4.8889
143	87	4.9055 ± 0.0049	4.9161 ± 0.0043	4.9140 ± 0.0041	4.9297 ± 0.0035		
144	88	4.9195 ± 0.0056	4.9338 ± 0.0051	4.9297 ± 0.0048	4.9488 ± 0.0041	4.9115	4.9128
145	89	4.9297 ± 0.0063	4.9466 ± 0.0056	4.9413 ± 0.0054	4.9626 ± 0.0046		
146	90	4.9424 ± 0.0071	4.9625 ± 0.0063	4.9555 ± 0.0061	4.9797 ± 0.0051	4.9263	4.9414
148	92	4.9660 ± 0.0086				5.0029	4.9752

[a] $\delta\langle r_c^2\rangle$ from Ref. [6] and r_c (^{138}Ba) from Ref. [1]. [b] $F = -3.163 \pm 0.144$ GHz/fm^2, $S/N = -0.707 \pm 0.109$ and $k = 0.97$ (see text), IS from Ref. [22] and r_c (^{138}Ba) from Ref.[21]. [c] $F = -3.897 \pm 0.189$ GHz/fm^2, $S/N = 2.649 \pm 0.27$ and $k = 0.97$ (see text), IS from Ref. [22] and r_c (^{138}Ba) from Ref. [1]. [d] F from multiconfiguration Dirac–Fock calculations [10], $S/N = 0.1 \pm 1.1$ and $k = 0.97$ (see text), IS from Ref. [22] and r_c (^{138}Ba) from Ref. [1].

Table 6
Charge radii (in fm) for Sm isotopes

A	N	F_{SE}[a]	$F_{\mu 1}$[b]	$F_{\mu 2}$[c]	$F_{\mu e^-}$[d]	HFB	GCM–GOA
136	74					5.0248	4.9716
138	76	4.9564 ± 0.0071				4.9633	4.9599
139	77	4.9521 ± 0.0071					
140	78	4.9450 ± 0.0071				4.9554	4.9578
141	79	4.9447 ± 0.0078					

Table 6 (*continued*)

A	N	F_{SE} [a]	$F_{\mu 1}$ [b]	$F_{\mu 2}$ [c]	$F_{\mu e^-}$ [d]	HFB	GCM–GOA
141	79	4.9497 ± 0.0071					
142	80	4.9484 ± 0.0069				4.939	4.953
143	81	4.9447 ± 0.0071					
144	82	4.9490 ± 0.0060	4.9520 ± 0.0060	4.9490 ± 0.0060	4.9490 ± 0.0060	4.9462	4.9637
145	83	4.9614 ± 0.0067	4.9636 ± 0.0076	4.9608 ± 0.0086	4.9637 ± 0.0094		
146	84	4.9758 ± 0.0070	4.9789 ± 0.0086	4.9768 ± 0.0106	4.9810 ± 0.0132	4.9583	4.9736
147	85	4.9857 ± 0.0088	4.9867 ± 0.0095	4.9843 ± 0.0123	4.9927 ± 0.0158		
148	86	5.0010 ± 0.0086	5.0035 ± 0.0106	5.0022 ± 0.0145	5.0110 ± 0.0198	4.9893	5.0034
149	87	5.0101 ± 0.0088	5.0104 ± 0.0115	5.0086 ± 0.0162	5.0218 ± 0.0222		
150	88	5.0312 ± 0.0090	5.0375 ± 0.0129	5.0382 ± 0.0190	5.0473 ± 0.0278	5.0381	5.0373
151	89	5.0471 ± 0.0098	5.0560 ± 0.0141	5.0580 ± 0.0213	5.0664 ± 0.0319		
152	90	5.0730 ± 0.0096	5.0916 ± 0.0157	5.0971 ± 0.0247	5.0979 ± 0.0387	5.1125	5.0964
153	91	5.0825 ± 0.0060	5.0995 ± 0.0166	5.1049 ± 0.0262	5.1091 ± 0.0412		
154	92	5.0956 ± 0.0098	5.1137 ± 0.0176	5.1198 ± 0.0282	5.1248 ± 0.0446	5.1215	5.1176

[a] $\delta\langle r_c^2\rangle$ from Ref. [6] and r_c (^{144}Sm) from Ref. [1]. [b] $F = -2.82 \pm 0.14$ GHz/fm^2, $S/N = -16.37 \pm 1.84$ and $k = 0.963$ (see text), IS from Ref. [25] and r_c (^{144}Sm) from Ref. [27]. [c] $F = -2.48 \pm 0.23$ GHz/fm^2, $S/N = -18.79 \pm 3.01$ and $k = 0.963$ (see text), IS from Ref. [25] and r_c (^{144}Sm) from Ref. [1]. [d] F and S/N from combined analysis [1] and r_c (^{144}Sm) from Ref. [1].

References

[1] G. Fricke, C. Bernhardt, K. Heilig, L.A. Schaller, L. Schellenberg, E.B. Shera, C.W. de Jager, At. Data Nucl. Data Tables 60 (1995) 177.
[2] J. Sauvage, J. Libert, B. Roussière, F. Le Blanc, J. Oms, A. Ouchrif, D. Verney, Rapport d'activité IPNO, 2000/2001, p. 32.
[3] B. Roussière, VI Latin American Symposium on Nuclear Physics and Applications, SLAFNAP6, 3–7 October 2005, Iguazu, Argentina, American Institute of Physics, in press.
[4] K. Bennaceur, P. Bonche, J. Meyer, C. R. Physique 4 (2003) 555.
[5] F. Le Blanc, et al., Phys. Rev. C 72 (2005) 034305.
[6] E.W. Otten, in: Treatise in Heavy-Ion Physics, vol. 8, 1989, p. 517, and references quoted in.
[7] H.-J. Kluge, W. Nortershauser, Spectrochimica Acta Part. B 58 (2003) 1031, and references quoted in.
[8] K. Heilig, H. Steudel, At. Data Nucl. Data Tables 14 (1974) 613.
[9] E.C. Seltzer, Phys. Rev. 188 (1969) 1916.
[10] G. Torbohm, B. Fricke, A. Rosén, Phys. Rev. A 31 (1985) 2038.
[11] W.H. King, Isotope Shifts in Atomic Spectra, Plenum, New York, 1984.
[12] F. Buchinger, P. Dabkiewicz, H.-J. Kluge, A.C. Mueller, E.W. Otten, Nucl. Phys. A 462 (1987) 305.
[13] M. Anselment, K. Bekk, A. Hanser, H. Hoeffgen, G. Meisel, S. Göring, H. Rebel, G. Schatz, Phys. Rev. C 34 (1986) 1052.
[14] P.E.G. Baird, et al., J. Phys. B 16 (1983) 2485.
[15] C. Piller, C. Gugler, R. Jacot-Guillarmod, L.A. Schaller, L. Schellenberg, H. Schneuwly, G. Fricke, T. Hennemann, J. Herberz, Phys. Rev. C 42 (1990) 182.
[16] J. Eberz, U. Dinger, G. Huber, H. Lochman, R. Menges, G. Ulm, R. Kirchner, O. Klepper, T.U. Kühl, D. Marx, Z. Phys. A 326 (1987) 121.
[17] R. Sifi, et al., VII International Workshop on Application of Lasers in Atomic Nuclei Research, LASER2006, May 29–June 01 2006, Poznan, Poland.
[18] B. Roussière, et al., ISOLDE Workshop, 6–8 February 2006, CERN, Geneva, Switzerland.
[19] E.B. Shera, M.V. Hoehn, G. Fricke, G. Mallot, Phys. Rev. C 39 (1989) 195.
[20] W. Borchers, E. Arnold, W. Neu, R. Neugart, K. Wendt, G. Ulm, Phys. Lett. B 216 (1989) 7.
[21] E.B. Shera, H.B. Wohlfahrt, M.V. Hoehn, Y. Tanaka, Phys. Lett. B 112 (1982) 124.
[22] K. Bekk, A. Andl, S. Göring, A. Hanser, G. Nowicki, H. Rebel, G. Schatz, Z. Phys. A 291 (1979) 219.
[23] A.C. Mueller, F. Buchinger, W. Klempt, E.W. Otten, R. Neugart, C. Ekström, J. Heinemeier, Nucl. Phys. A 403 (1983) 234.

[24] V.S. Letokhov, V.I. Mishin, S.K. Sekatsky, V.N. Fedoseyev, G.D. Alkhazov, A.E. Barzakh, V.P. Denisov, V.E. Starodubsky, J. Phys. G 18 (1992) 1177.
[25] J.G. England, I.S. Grant, J.A. Griffith, D.E. Evans, D.A. Eastham, G.W.A. Newton, P.M. Walker, J. Phys. G 16 (1990) 105.
[26] H. Brand, B. Seibert, A. Steudel, Z. Phys. A 296 (1980) 281.
[27] R.J. Powers, P. Barreau, B. Bihoreau, J. Miller, J. Morgenstern, J. Picard, L. Roussel, Nucl. Phys. A 316 (1979) 295.
[28] P. Barreau, L. Roussel, R.J. Powers, Nucl. Phys. A 364 (1981) 446.
[29] I. Angeli, At. Data Nucl. Data Tables 87 (2004) 185.
[30] D. Gogny, in: J. De Boer, H.J. Mang (Eds.), Proceedings of the International Conference on Nuclear Physics, Munich, 1973, North-Holland, Amsterdam, 1973;
D. Gogny, in: G. Ripka, M. Porneuf (Eds.), Proceedings of the International Conference on Nuclear Selfconsistent Fields, Trieste, 1975, North-Holland, Amsterdam, 1975.
[31] J. Dechargé, D. Gogny, Phys. Rev. C 21 (1980) 1568.
[32] J.-F. Berger, M. Girod, D. Gogny, Comput. Phys. Commun. 63 (1991) 365.
[33] M. Girod, B. Grammaticos, Phys. Rev. C 27 (1983) 2317.
[34] M. Bertozzi, et al., Phys. Lett. B 41 (1972) 408.
[35] J.-P. Delaroche, et al., Phys. Rev. C 50 (1994) 2332.
[36] J. Libert, M. Girod, J.-P. Delaroche, Phys. Rev. C 60 (1999) 054301.
[37] J.-P. Delaroche, M. Girod, H. Goutte, J. Libert, Nucl. Phys. A 771 (2006) 107.
[38] K. Kumar, M. Baranger, Nucl. Phys. A 92 (1967) 608.
[39] S. Raman, C.W. Nestor, P. Tikkanen, At. Data Nucl. Data Tables 78 (2001) 64.
[40] http://www.nndc.bnl.gov/ensdf/za_form.jsp.